ATMOSPHERIC ENVIRONMENT: X 5 (2020) 100064

Contents lists available at ScienceDirect

Atmospheric Environment: X

journal homepage: http://www.journals.elsevier.com/atmospheric-environment-x

Reconciling Gaussian plume and Computational Fluid Dynamics models of particulate dispersion

G.M.D. Joseph , D.M. Hargreaves *, I.S. Lowndes

Faculty of Engineering, University of Nottingham, Nottingham, NG7 2RD, UK

ARTICLE INFO

Keywords:
Dispersion
CFD
Gaussian plume
Particulates

ABSTRACT

Computational Fluid Dynamics (CFD) is increasingly used to model particulate dispersion in situations where Gaussian Dispersion models are inappropriate or inaccurate. However, there is evidence which indicates that many CFD models under-predict lateral plume spread. This paper aims to address this by implementing a strategy which incorporates wind direction variability into CFD models using a formulation which is also used in the UK-ADMS plume spread module. In the present work, a series of CFD simulations are run at various wind angles. The outputs from these simulations are weighted using a Gaussian probability density function and combined to produce a plume. The standard $k-\varepsilon$ model has been employed to solve the RANS equations of the flow field for stable, neutral and unstable atmospheric stabilities, coupled with the Lagrangian Particle tracking model to model dispersion. By comparing the CFD accretion profiles to UK-ADMS dry deposition results, it is observed that the proposed modelling methodology produces lateral spreading of the plume which is comparable to that obtained using UK-ADMS. However, the Lagrangian integral time scale constant, c_L, which governs the influence turbulence has on the dispersion, must also be modified to bring absolute values of accretion rates in line with those observed in UK-ADMS.

1. Introduction

Gaussian models have been found to overestimate the long range transport of particulates because, according to Cowherd et al. (2006), the model algorithms do not adequately represent plume depletion due to removal mechanisms such as gravitational settling, deposition and agglomeration. Indeed, field studies by Watson and Chow (2000) and Countess (2001) demonstrate that coarser fractions of fugitive dust, namely PM 2.5 and above, are rapidly removed from the air stream by gravitational settling and deposition within 100 m of the emission source. The dissonance between Gaussian model deposition predictions and field observations becomes even more pronounced in low wind or calm conditions, where the intrinsic limitations of Gaussian models such as the assumption of plume dispersion dominated by advective transport, render their predictions unreliable (Arya, 1995). Gaussian models are also severely challenged by terrain complexity and orographical effects, and several studies (Lowndes et al., 2008; Silvester et al., 2009; Di Sabatino et al., 2007), have recognised that Computational Fluid Dynamics (CFD) models offer superior resolution of flow regimes perturbed by complex topography. Further complications are seen when attempting to model dispersion in the urban landscape, where the presence of buildings challenges the Gaussian approximation, certainly in the near-field (Tominaga and Stathopoulos, 2013; Lateb et al., 2016; Toja-Silva et al., 2017, 2018).

However, whilst CFD models are gaining increasing popularity in atmospheric dispersion applications, they have not superseded conventional Gaussian models as the preferred numerical tool for pollutant dispersion because, quite apart from their computational expense and the challenges of maintaining homogeneous velocity, turbulence and temperature profiles along the fetch, CFD models are unable to produce lateral spreading of the pollutant plume beyond that which is attributable to boundary layer turbulence, since directional variability of the wind due to mesoscale effects is not typically a feature of these models.

A methodology to incorporate wind direction variability in CFD models of the neutral Atmospheric Boundary Layer (ABL) was first proposed in work by Quinn et al. (2001), where wind direction fluctuations were represented by nine CFD simulations, each corresponding to 5° angular increments of wind variation within a range of −20° to 20°. Weighted summations of the simulations were subsequently used to account for the effects of wind direction variability on plume dispersion.

* Corresponding author.
E-mail addresses: david.hargreaves@nottingham.ac.uk (D.M. Hargreaves), ian.lowndes@nottingham.ac.uk (I.S. Lowndes).

https://doi.org/10.1016/j.aeaoa.2020.100064

Available online 6 February 2020

A more recent paper by Vervecken et al. (2013), builds on the Quinn et al. (2001) methodology by proposing a decomposition of wind direction variability into one component due to boundary layer turbulence and another due to external causes of wind direction variability. They assert that the latter component can be derived from field measurements, once the former is deduced from the turbulence closure equations because variability due to boundary layer turbulence is already represented in the turbulence model. Their reasoning appears to be in line with the premise of the empirically derived formulation by Moore (1976) which is used in dispersion models such as UK-ADMS to account for the lateral spreading of the pollutant plume. The Moore (1976) formulation also decouples the contribution of boundary layer turbulence from that of wind variability arising from larger scale atmospheric motions.

This study is distinct from previous studies by Quinn et al. (2001) and Vervecken et al. (2013) because in addition to the neutral ABL, the stable and unstable ABL are also considered, thus the methodology is shown to be also applicable to these stability classes. Moreover, this study differs in that the dispersion of a particulate plume consisting of four particle size fractions representative of typical total suspended particle (TSP) emissions is considered. An Euler-Lagrange approach has been adopted here for modelling the dispersion of particulates in the computational domain. Thus, the Lagrangian discrete phase model has been selected to provide stochastic tracking of the particles. Quinn et al. (2001) and Riddle et al. (2004) have noted that predictions of gaseous dispersion using this model were superior to those of the advection-diffusion (AD) model. Moreover, Thomson (1987) indicated that stochastic models are more appropriate tools for modelling near-source dispersion of particles entrained in complex flows. In the stochastic model, particle-eddy interactions are influenced by the Lagrangian integral time, which the user is able to modify through the time scale constant c_L. Consequently, a range of c_L have been applied in this work to adjust the dispersive characteristics of the FLUENT plume, thereby facilitating comparison to UK-ADMS predictions.

The use of UK-ADMS in this work is predicated on its widespread use as an operational dispersion model. It has been validated against datasets from all around the world and has proved highly accurate particularly over flat terrain, which is used in the present work (Riddle et al., 2004). Not only that, it includes models for wind direction variability, particle deposition and can model a wide range of stability classes and wind speeds – all of which are required in the present work. Essentially, the goal here is to produce a FLUENT model that can reproduce the UK-ADMS predictions, given the correct choice of governing equations, boundary conditions, model parameters and solution methodology. As such, this is not a validation against experimental data, rather it is a verification against a validated model. For validation, one would look to using the results from, for example, Quinn et al. (2001). However, obtaining such results is difficult and in any case includes a building in the near-field, which the present work does not, so as not to detract from the focus on the effects of wind direction variability.

The proposed methodology for incorporating wind direction variability into the CFD model, relies on parametrisation of the standard deviation of wind direction in a manner which captures the dependency of wind direction variability on the mean wind velocity and the averaging time. It is envisioned that this methodology could be applied in the absence of wind variability measurements.

2. Directional variability of the wind

Dispersion models rely on the input of meteorological data, which are typically averaged over time scales ranging from several minutes to 1 h. At these time scales, it becomes necessary to consider the implications of atmospheric motions which exceed the turbulence scale. Fig. 1 illustrates that microscale turbulence is characterized by time scales of up to 50 min and length scales under 50 m. The dispersion of a pollutant plume in the vertical direction is primarily due to turbulent mixing

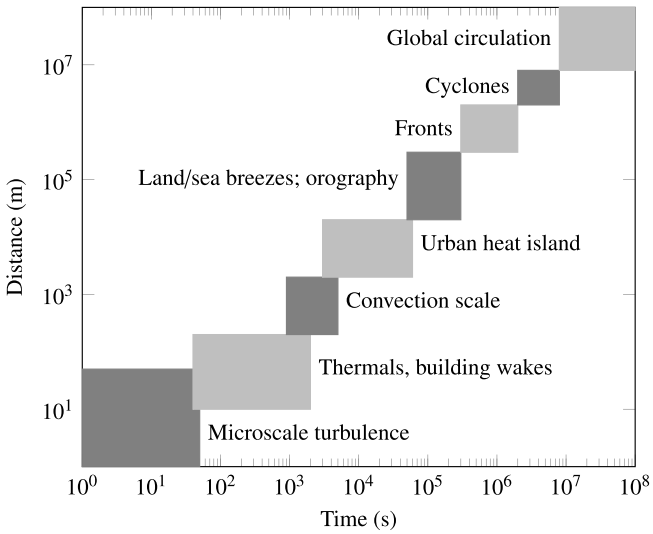

Fig. 1. Spatial and temporal scales of turbulence, adapted from Isaksen et al. (2009).

across the boundary layer depth, however the plume is not confined by the mixing height in the horizontal direction and in this plane, the spread of the plume is influenced by mesoscale and in some cases synoptic scale atmospheric phenomena, which produce low frequency oscillations of the wind (Vickers et al., 2008; Davies and Thomson, 1999).

Many atmospheric phenomenon can give rise to wind direction variability: gravity waves, drainage flows, topographic effects and cloud cover variations are among the likely causes suggested by Davies and Thomson (1999) and Mahrt (2010). Wind direction variations occur for all classes of atmospheric stability and terrain, but it is noted in work by Anfossi et al. (2005) that oscillations of the wind direction dominate the flow and are therefore the primary drivers of plume dispersion in stable, low wind conditions where turbulent mixing is suppressed. To dispel any ambiguity which may arise over what is meant by low wind conditions, the definition provided by Deaves and Lines (1998) is invoked here, where low wind conditions are defined as instances where the mean wind speed, $\overline{u}$, is less than or equal to the root mean square horizontal turbulent velocity, σ_u. This typically equates to wind speeds below 1 ms^{-1} in convective conditions and 0.5 ms^{-1} in neutral and stable conditions.

In order to account for the meandering motions of the wind in the CFD numerical model, one must first arrive at an appropriate parametrisation for the wind direction variability in the absence of field measurements. A study by Mahrt (2010) examined surface wind variability for the stable boundary layer and advanced a formulation for the standard deviation of wind variability in low wind conditions, $\sigma_{\delta wd}$, which he termed the *wind direction variability*. An example of his findings for a nocturnal, stable ABL are shown in Fig. 2. He proposed an expression that reflects the inverse proportionality between wind direction variability (measured in degrees) and wind speed, V,

$$\sigma_{\delta_{wd}} = \frac{A}{V_{mod}} + BV^n, \tag{1}$$

where V_{mod} is a modified velocity scale

$$V_{mod} = \sqrt{V^2 + V_{sg}^2}, \tag{2}$$

which prevents the wind directional variability from becoming too large at low wind speeds by the appropriate choice of V_{sg}. Mahrt (2010) suggests values for A of 10° m s^{-1} for complex terrain and 5° m s^{-1} for flat. The second term in Equation (1) accounts for those contributions to wind direction variability that do not decrease with increasing wind speed, such as turbulence wind direction variations. It also represents

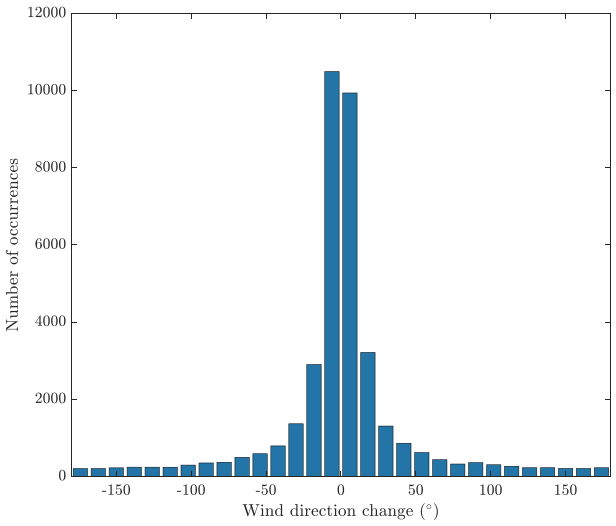

Fig. 2. Distribution of the wind direction variability at a height of 2 m at 1 min intervals in a nocturnal ABL, adapted from Mahrt (2010).

enhancement of wind direction variability by complex terrain. The exponent n takes a value of 0.5, while $B = 2^{\circ}$ for complex terrain and 0.5° for flat.

UK-ADMS imposes a limit of $\pm\pi/6$ to wind direction variability in the Moore (1976) formula to restrict wind direction variability to realistic values in low wind conditions, thus the component of wind direction variability due to motions which exceed the turbulence scale is given by

$$\sigma_\theta = 0.065\sqrt{\frac{7T_A}{U_{10}}}, \tag{3}$$

for $-\pi/6 \leq \sigma_\theta \leq \pi/6$, where σ_θ represents the wind direction variability in radians, T_A is the averaging time in hours and U_{10} is the wind velocity in ms^{-1} at a reference height of 10 m above the ground.

The observation that the wind direction variability increases with averaging time is represented in empirical formulae by Moore (1976) and also emerges in work by Davies and Thomson (1999) and Mahrt (2010), although the Mahrt (2010) generalisation does not capture this correlation. A 1 h averaging time is used here, because meteorological data is usually supplied to dispersion models in the form of hourly averaged measurements. However, since air quality standards can require assessment of pollutant concentrations at various averaging times, it is therefore useful to adopt a formulation for wind variability which captures the dependence on averaging time. On this basis, the Moore (1976) generalisation has been selected here for parametrisation of the standard deviation of wind variability and consequently, UK-ADMS (Version 5.0) is used as a platform for assessing the improvements in lateral plume spreading obtained using the proposed CFD modelling methodology. Conversely, it is seen in Davies and Thomson (1999) and Mahrt (2010) that there is no further decrease in wind variability with increasing wind speed above 5 ms^{-1}. It appears that wind variability remains approximately constant once a 5 ms^{-1} velocity threshold is reached. Hence, for reference wind speeds exceeding 5 ms^{-1} a nominal $\sigma_{\delta\mathrm{wd}}$ of 5° is applied.

Despite their work being concerned with urban wind flow patterns, Wise et al. (2018) used CFD to look at the consequences of small variations in the wind direction in a small area of Singapore. They found that the flow was very sensitive to wind direction but did not attempt to conduct any averaging process, as we do here. However, Sousa and Gorlé (2019) have used a Bayesian inference method to estimate the boundary conditions for CFD simulations of the urban environment from field measurements. The method allows the number of simulations (varying wind speed and direction) to be reduced while maintaining the predictive accuracy of the results.

3. Methodology

This section of the paper deals almost exclusively with the setup of the CFD simulations and does not include details of the UK-ADMS simulations. Details of those can be found in § 3.2 of Joseph (2016).

3.1. The computational domain

The computational domain consisted of an empty rectangular box of length, $L = 425$ m, height, $H = 180$ m and width, $B = 200$ m as shown in Fig. 3. Whilst the length and height were selected to match the extents of the fetch used in Alinot and Masson (2005), the width of 200 m was chosen to provide adequate lateral grid space to contain the plume spread and wind direction changes. The domain was meshed with hexahedral cells ($164 \times 200 \times 110$; length $\times$ width $\times$ height). The height of the wall adjacent cell was 0.6 m and 110 cells with a growth ratio of 1.02 were used to discretise the vertical direction.

3.2. Governing equations

The standard, steady-state $k-\varepsilon$ model has been used for which the continuity, momentum and energy equations are

$$\int_A u_i n_i \, \mathrm{d}A = 0, \tag{4}$$

$$\int_A \rho u_j u_i n_i \, \mathrm{d}A = -\int_A p\delta_{ij} n_i \, \mathrm{d}A + \int_A \tau_{ij} n_i \, \mathrm{d}A + \int_V \rho g_i \, \mathrm{d}V, \tag{5}$$

$$\int_A \rho c_p T u_i n_i \, \mathrm{d}A = \int_V \rho u_i g_i \mathrm{d}V + \int_A \left[u_j \tau_{ij} + \frac{c_p \mu_t}{\sigma_t}\left(\frac{\partial T}{\partial x_i} - \frac{g_i}{c_p}\right)\right] \mathrm{d}A, \tag{6}$$

where p is the pressure, u_i and g_i are the i^{th} components of the flow velocity and gravitational acceleration respectively, A denotes the outer surface area of the control volume V and n_i is the unit vector normal to the surface, A. ρ is the fluid density, δ_{ij} is the Kronecker delta operator, τ_{ij} is the viscous stress tensor, c_p is the specific heat capacity of air at constant pressure and T is the temperature.

Transport equations for turbulent kinetic energy, k, and its dissipation rate, ε are also solved,

$$\int_A \rho k u_i n_i \, \mathrm{d}A = \int_V \left[P_t - \rho\varepsilon + G_b\right] \mathrm{d}V + \int_A \frac{\mu_t}{\sigma_k}\frac{\partial k}{\partial x_i} n_i \, \mathrm{d}A \tag{7}$$

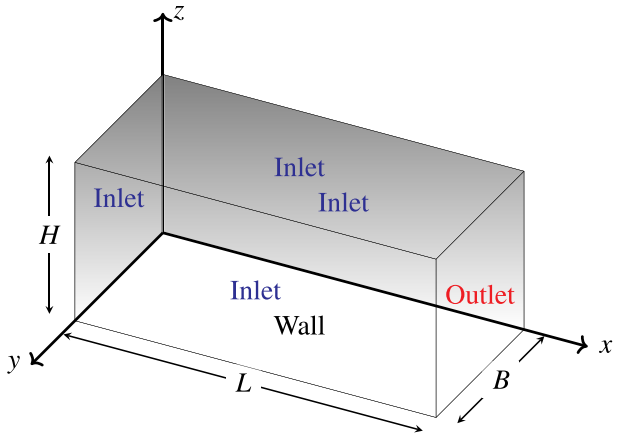

Fig. 3. The domain, showing dimensions, boundary condition types and coordinate system.

$$\int_A \rho\varepsilon u_i n_i \, dA = \int_A \frac{\mu_t}{\sigma_\varepsilon}\frac{\partial \varepsilon}{\partial x_i} n_i \, dA + \int_V \left[C_{\varepsilon 1}\frac{\varepsilon}{k}(P_t + (1 - C_{\varepsilon 3})G_b) - C_{\varepsilon 2}\rho\frac{\varepsilon^2}{k}\right] dV, \tag{8}$$

where μ_t is the turbulent viscosity. P_t and G_b are the shear and buoyancy contributions to the production or removal of turbulent kinetic energy, respectively and are expressed by

$$P_t = \mu_t\left(\frac{\partial u_i}{\partial x_j} + \frac{\partial u_j}{\partial x_i}\right)\frac{\partial u_i}{\partial x_j}, \tag{9}$$

$$G_b = \beta g_i \frac{\mu_t}{\sigma_t}\left(\frac{\partial T}{\partial x_i} - \frac{g_i}{c_p}\right). \tag{10}$$

In the $k - \varepsilon$ model, the turbulence viscosity is given by

$$\mu_t = \rho C_\mu \frac{k^2}{\varepsilon}. \tag{11}$$

in addition, C_μ, $C_{\varepsilon 1}$, $C_{\varepsilon 2}$ and $C_{\varepsilon 3}$ are model constants and β is the thermal volumetric expansion coefficient of the air. σ_k and σ_ε are the Prandtl numbers for turbulent kinetic energy and turbulent dissipation rate. Furthermore, these model coefficients have been changed from the original Jones and Launder (1973) values as shown in Table 1. The missing number for $C_{\varepsilon 3}$ in the table is because this is calculated from a polynomial curve fit for which the reader is referred to Alinot and Masson (2005). Source terms have also been introduced to the k, ε and energy equations to account for the effects of thermally induced buoyancy.

3.3. Lagrangian Particle tracking

In ANSYS FLUENT, the Lagragian Particle tracking (LP) model (also called the DPM model in FLUENT) determines the trajectory of discrete particles by integrating the particle force balance equation written in a Lagrangian reference frame,

$$\frac{d\mathbf{u}_p}{dt} = \mathbf{F}_D + \frac{\rho_p - \rho}{\rho_p}\mathbf{g} \tag{12}$$

where $\mathbf{u}$ is the local fluid velocity, $\mathbf{u}_p$ is the velocity of the particle, $\mathbf{F}_D$ is the drag force per unit mass acting on the particle. The acceleration due to gravity is $\mathbf{g}$, and ρ and ρ_p are the fluid and particle densities respectively. The drag force is a function of the particle Reynolds number based on the relative velocity between the particle and the local fluid, $\mathbf{u} - \mathbf{u}_p$, and the particle diameter, d_p.

In order to predict dispersion of dust particles injected into a turbulent atmosphere, the Discrete Random Walk (DRW) stochastic model has been employed here. This model requires the instantaneous fluctuating component of the flow field velocity $\mathbf{u}'(t)$. Thus the particle trajectory is determined by integrating Equation (12), using the instantaneous fluid velocity $\overline{\mathbf{u}} + \mathbf{u}'(t)$. In this model, it is assumed that the turbulence is isotropic and that the individual components of the fluctuating velocity are related to the turbulent kinetic energy as

$$u' = v' = w' = \zeta\sqrt{2k/3}, \tag{13}$$

where ζ is a normally distributed random number, representing the Gaussian distribution of the fluctuating velocity components.

T_L is the Lagrangian integral time scale computed from the following expression,

$$T_L = c_L\frac{k}{\varepsilon}. \tag{14}$$

where c_L is given a default value of 0.15 for the $k - \varepsilon$ model with the turbulent kinetic energy and its dissipation rate in being found from the Eulerian solution of the flow field (Equations (7) and (8)). It can be shown using this approach that the particle diffusivity is given by $\overline{u_i' u_j'} T_L$, indicating that a higher value of c_L results in a greater dispersion of the particles.

The DRW model computes the fluctuating velocity component, Equation (13), and holds it constant for discrete time intervals corresponding to the shorter of the particle eddy crossing time, t_{cross}, and the characteristic lifetime of the turbulent eddies, t_e given by,

$$t_{cross} = -\tau\ln\left[1 - \left(\frac{L_e}{\tau\,|\mathbf{u} - \mathbf{u}_p|}\right)\right], \tag{15}$$

$$t_e = -T_L \log r, \tag{16}$$

where τ is the particle relaxation time, L_e is the eddy length scale and r is a uniform random number between 0 and 1.

Gorlé et al. (2009) observed that the value of the constant c_L has an important effect on predictions of concentration which utilise the stochastic model. As a result, they recommended sensitivity tests to ascertain appropriate values of c_L. The Lagrangian integral time scale is correlated to the turbulent dissipation rate for turbulent eddies in the inertial sub-range according to

$$T_L = \frac{2\sigma_i^2}{C_o\varepsilon} \tag{17}$$

where σ_i is the velocity variance component and C_o represents the Kolmogorov constant which ranges between 3 and 10 (Degrazia and Anfossi, 1998). The turbulent kinetic energy can be written in terms of the velocity variance components as

$$k = \frac{1}{2}\left(\sigma_u^2 + \sigma_v^2 + \sigma_w^2\right). \tag{18}$$

Recalling the assumption of isotropic turbulence which underpins the $k - \varepsilon$ model, $\sigma_u^2 = \sigma_v^2 = \sigma_w^2$, thus:

$$k = 1.5\sigma_u^2 \tag{19}$$

Thus equation (17) can be rearranged to give T_L in terms of turbulent kinetic energy and its dissipation rate,

$$T_L = \frac{4}{3C_o}\frac{k}{\varepsilon}, \tag{20}$$

In the DPM model, T_L is determined by matching the diffusivity of the particles to the scalar diffusion rate predicted by the turbulence model, thus the default c_L value of 0.15 correlates to a C_o value of 8.5 using Equation (20) and falls within the range of C_o values suggested by Degrazia and Anfossi (1998). Equation (20) has also been presented in the work of Gorlé et al. (2009) and subsequently applied to arrive at appropriate values of c_L.

3.4. Boundary conditions

To obtain homogeneous profiles of the ABL, stability modified inlet profiles (Richards and Hoxey, 1993) and a temperature profile equation have been imposed at the domain inlets based on work by Alinot and Masson (2005),

Table 1
$k - \varepsilon$ turbulence closure model constants.

Model	C_μ	$C_{\varepsilon 1}$	$C_{\varepsilon 2}$	$C_{\varepsilon 3}$	σ_k	σ_ε	σ_T
Jones and Launder (1973)	0.09	1.44	1.92	1.0	1.0	1.3	1.0
Alinot and Masson (2005)	0.0333	1.176	1.92	–	1.3	1.0	1.0

$$u(z)=\begin{cases}\dfrac{u_*}{\kappa}\left[\ln\left(\dfrac{z}{z_0}\right)+\ln\left(\dfrac{8\varphi_m^4}{(\varphi_m+1)^2(\varphi_m^2+1)}\right)-\dfrac{\pi}{2}+2\tan^{-1}\left(\dfrac{1}{\varphi_m}\right)\right] & L<0,\\ \dfrac{u_*}{\kappa}\left[\ln\left(\dfrac{z}{z_0}\right)+\varphi_m-1\right] & L>0,\end{cases} \tag{21}$$

$$T(z)-T_w=\begin{cases}\dfrac{T_*}{\kappa}\left[\ln\left(\dfrac{z}{z_0}\right)-2\ln\left(\dfrac{1}{2}\left(1+\varphi_m^{-2}\right)\right)\right]-\dfrac{g}{c_p}(z-z_0) & L<0,\\ \dfrac{T_*}{\kappa}\left[\ln\left(\dfrac{z}{z_0}\right)+\varphi_m-1\right]-\dfrac{g}{c_p}(z-z_0) & L>0,\end{cases} \tag{22}$$

where κ is the von Karman constant, generally taken as 0.42, T_w is the surface temperature, z_0 is the aerodynamic roughness length, u_* and T_* are the surface layer scaling velocity and temperature respectively,

$$u_*=\sqrt{\frac{\tau}{\rho}}, \tag{23}$$

$$T_*=\frac{q_w}{\rho c_p u_*}, \tag{24}$$

with τ as the surface shear stress and q_w as the surface heat flux. φ_m and φ_ε (the latter used later in Equations (28) and (29)) are the Bussinger-Dyer similarity functions which define fluxes of velocity and turbulence in the constant shear stress surface layer as functions of height based on Monin-Obukhov (M-O) similarity theory (Kaimal and Finnigan, 1994; Luketa-Hanlin et al., 2007). The similarity functions are given by,

$$\varphi_m=\begin{cases}\left(1-16\dfrac{z}{L}\right)^{-1/4} & L<0,\\ 1+\dfrac{5}{L} & L>0,\end{cases} \tag{25}$$

and

$$\varphi_\varepsilon=\begin{cases}1-\dfrac{z}{L} & L<0\\ \varphi_m-\dfrac{z}{L} & L>0\end{cases}. \tag{26}$$

where L is the Monin-Obukhuv length,

$$L=\frac{-u_*^3\rho c_p T_w}{\kappa g q_w}. \tag{27}$$

For the turbulence profiles at the inlet, the following are used

$$\varepsilon(z)=\frac{u_*^3}{Kz}\varphi_\varepsilon, \tag{28}$$

$$k(z)=\sqrt{\frac{\mu_t\varepsilon}{\rho C_\mu}}=5.48u_*^2\left[\frac{\varphi_\varepsilon}{\varphi_m}\right]^{\frac{1}{2}}, \tag{29}$$

Velocity inlets were specified at the domain inlet, top and side boundaries (Fig. 3) using the modified Richards and Hoxey (1993) profiles for the u and v-components of the flow velocity, with a pressure outlet at the exit. The standard rough wall treatment was adopted for the ground boundary where the roughness height, K_s, was given by,

$$K_s=20\,z_0 \tag{30}$$

as recommended in work by Hargreaves and Wright (2007). The aerodynamic roughness length, z_0, was taken as 0.01 m. Thus, the height of the wall adjacent cell (0.6 m) was sufficient to satisfy the requirement of $z_p > K_s$ specified by Blocken et al. (2007), where z_p is the height to the centroid of the wall-adjacent cell. The pressure-based solver has been implemented along with the SIMPLEC algorithm for pressure-velocity coupling, the PRESTO interpolation scheme has been selected for pressure discretisation and second order upwind differencing schemes have been chosen for other flow field equations.

In the DPM model, an injection file was used to introduce a particulate emissions source. In essence, particles were injected into 5 m × 5 m × 5 m cuboid source volume, centred at (52.5, 100, 12.5) from points spaced at intervals of 0.2 m, giving a total of 62,500 particles. In order to put this number into perspective, Riddle et al. (2004) used a total of 10,000 particles for their comparison between UK-ADMS and the FLUENT DPM model. The size and location of the source can be viewed in the context of the modelling of dust dispersion in a UK quarry from which the present work is extracted (Joseph, 2016; Joseph et al., 2018).

A typical quarry blasting event would liberate 25,000 tonnes of limestone rock. Michigan Department of Environmental Quality (2004) suggests a PM_{10} blast emission factor of 0.036 kg/tonne from which was derived a total suspended particulate (TSP) emission rate of 0.568 kg s^{-1}. This mass flow rate was evenly divided between the 62,500 particle tracks, each with a mass flow rate, $\dot{m}_p$.

The particle density was taken as 2600 kg m^{-3} – the density of the parent rock. The particle size distributions are given in Table 2.

The particles were injected at rest (preliminary tests showed that dispersion was largely independent of the initial particle velocity because of the short stopping distances of the particles). The accretion rates of the particulates at the ground wall boundary were used to assess lateral plume spread as these can be directly compared to dry deposition rates from the UK-ADMS model. The accretion rate, R_{acc}, for a face on the ground wall is the sum of mass flow rates of the N_p particles which impact on it, divided by its area, A_{face}, as

$$R_{acc}=\sum_{p=1}^{N_p}\frac{\dot{m}_p}{A_{face}}. \tag{31}$$

3.5. Meteorological conditions

The meteorological conditions adopted in this study are representative of the three stability classes listed in Table 3. Values of the Monin-Obukhuv length, L, have been selected to coincide with the middle of the ranges suggested by Barthelmie (1999) and Woodward (1999) for the stable and unstable atmosphere respectively. Wind speeds at a reference height of 10 m were derived from the Pasquill-Gifford-Turner (PGT) scheme for the three stability classes. Using a roughness length which represents surface roughness for a flat open plain, the Monin-Obukhuv similarity theory was applied to determine the heat flux. The wind direction variability $\sigma_{\delta wd}$, was computed from Equation (3) to the nearest degree, however, for $u_{10} > 5$ ms^{-1}, $\sigma_{\delta wd}$ was taken as 5°.

A reference wind speed of 3 ms^{-1} has been chosen to represent the stable case. Thus, the wind velocity profile is representative of the weak wind conditions generally experienced in the stable ABL, because as the wind speed increases above 5 ms^{-1} with a corresponding increase in mechanical turbulence, the atmospheric stability tends towards the neutral case. The value of 3 ms^{-1} is also sufficiently high so as not to compromise the reliability of the Gaussian model.

Table 2
Particle size distributions.

Particle diameter (μm)	Mass Fraction
75	0.3
30	0.2
10	0.5
2.5	0.05

Table 3
Meteorological parameters.

Stability Class	PGT Class	u_{10} (ms^{-1})	$\sigma_{\delta wd}$ (°)	L (m)	z_0 (m)	q_w (W m^{-2})	T_w (K)
Unstable	A	5	5	−100	0.01	28.41	298
Neutral	D	8	5	∞	0.01	0	285
Stable	F	3	6	100	0.01	−4.17	283

3.6. Accretion versus dry deposition

In UK-ADMS, dry deposition is modelled using a Eulerian approach which relies on the calculation of a deposition velocity that brings particles in contact with the wall. Therefore the dry deposition flux, F_{dry}, which is defined as the rate of accumulation of particulate mass per unit wall surface area is calculated from

$$F_{\text{dry}} = v_d\, C(c, y, 0), \tag{32}$$

where v_d is the deposition velocity and $C(x, y, 0)$ is the near-surface concentration of particulates. The deposition velocity is a function of the particle properties (diameter, density, shape), the characteristics of the ground and the wind speed. Its value is held constant throughout any given simulation when the terrain is homogeneous, as it the case in the present work. Further, the deposition velocity is formed from a diffusive part, v_d', which models the effects of turbulent and a gravitational part, v_t, which accounts for the settling of the particle under the influence of gravity

$$v_d = \frac{v_t}{1 - \exp(-v_t/v_d')}. \tag{33}$$

In FLUENT, the accretion rate in the DPM model is the equivalent of the dry deposition flux in ADMS. However, differences occur in the route to their calculation: in the DPM model, accretion rates are calculated from individual particle track impacting on the individual faces of the ground wall. In ADMS, the deposition velocity (and hence flux) are calculated from mean statistics and therefore does not exhibit the scatter of the inherently stochastic DPM approach.

The particulate concentration in the plume in the ADMS model is attenuated by means of a depletion factor as material is removed at the ground. This surface is assumed to act as a perfect sink for particulates so that dry deposition is an irreversible process with particles incapable of being re-suspended. This tallies with the DPM approach where particles are removed via the so-called "trap" boundary condition at the wall. Throughout what follows, accretion rates/dry deposition fluxes have units of kg m^{-2} s^{-1}.

4. Results and discussion

4.1. Homogeneous ABL profiles

Before we consider the dispersion and subsequent accretion of the particles, a discussion of the nature of the three stability classes is useful. The flow fields in each case are calculated prior to the DPM simulations because the latter is essentially a post-processing operation on a fixed background flow. In Fig. 4, homogeneous profiles of non-dimensionalised velocity, temperature, turbulent kinetic energy and turbulent dissipation rate,

$$\frac{u}{u_*}, \quad \frac{(T - T_w)}{T_w}, \quad \frac{k}{u_*^2}, \text{ and } \frac{\varepsilon\, z_{\text{ref}}}{u_*^3}.$$

halfway along the domain are shown, with z_{ref} the reference height of 10 m. The profiles were also recorded at the inlet to the domain, but are

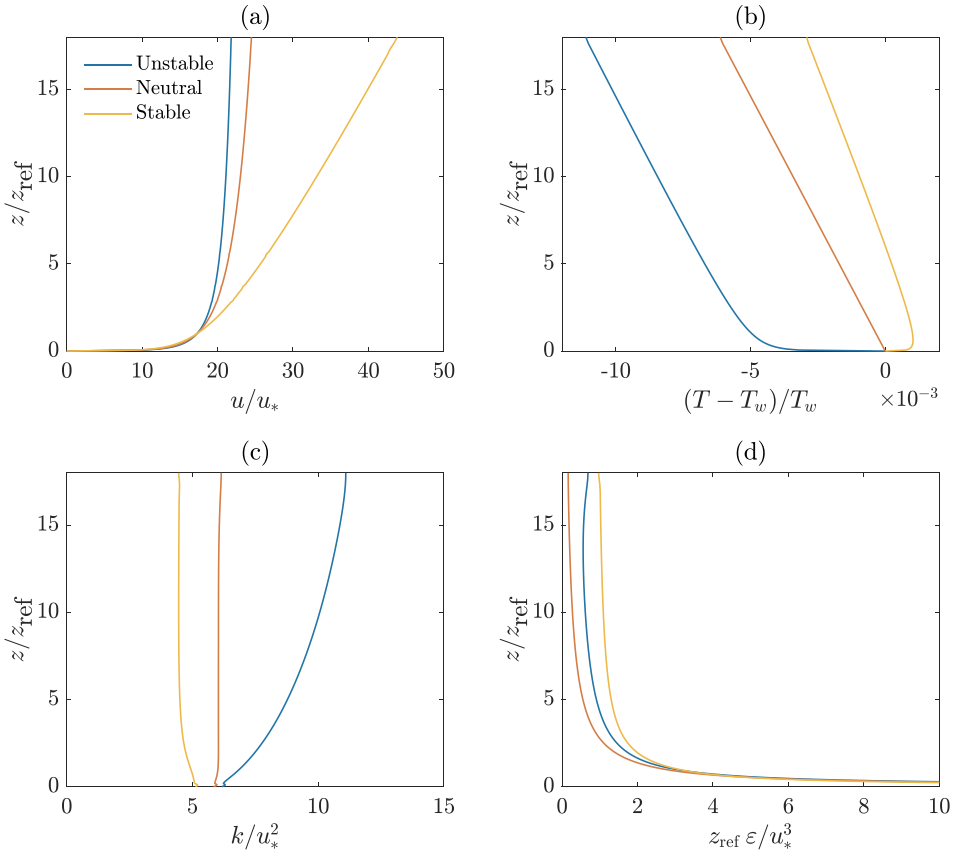

Fig. 4. Vertical profiles of non-dimensionalised (a) u-component of velocity, (b) temperature, (c) turbulent kinetic energy and (d) turbulent dissipation rate for unstable, neutral and stable atmospheres at $x = L/2$.

not plotted because they all lie on top of the profiles seen in Fig. 4. That is, however, apart from the unstable turbulent dissipation rate, which exhibits a slight increase near the top of the domain. Since the dispersion is predominantly in the lower part of the domain (due to particle settling), this was not seen as an important issue. On the whole, then, it can be deduced that homogeneous atmospheric profiles have been imposed on the domain, albeit for a relatively short one. In defence of the use of such a short domain, experience of this dispersion and settling process is that the bulk of the particles settle out over these kind of length scales (Joseph et al., 2018). The inlet profiles were also compared with their analytical form (Equations (21)–(29)) and found to agree exactly.

Having established the quantitative agreement of the profiles with the work of Alinot and Masson (2005), it is worth briefly discussing the qualitative nature of the profiles in Fig. 4. Plot (a) displays the characteristic profiles of the three classes of stability, with the sharpest increase being for the unstable ABL. In terms of the temperature gradients, plot (b), we see the greatest negative gradient for the unstable ABL, with a brief positive gradient seen near the ground for the stable environment. As expected, the highest levels of turbulence are seen for the unstable ABL in plot (c).

4.2. Fixed wind direction simulations

In order to provide a baseline against which the variable wind directions and modified c_L values can be compared, a comparison was made between a single $\theta = 0^\circ$ FLUENT simulation and ADMS (with wind variability turned on). Recall that the default value of the Lagrangian time scale constant, c_L, is 0.15 in all variants of the $k-\varepsilon$ model in FLUENT. However, the results presented in this section are for a value of 0.30 because the effects of averaging are emphasised with this value. A discussion of the effects of changing c_L is presented in Section 4.4.

The results of this comparison are shown for the neutral case in Fig. 5. As can be seen from plot (a) in the figure, which shows the accretion rate along the centreline of the plume, the stochastic nature of the DPM simulation is apparent. The accretion rates are scattered – a scatter that becomes more pronounced downstream as the finite number of particles disperses in the plume and fewer and fewer impact on the individual faces of the ground wall. Clearly the CFD predictions of accretion rate are a factor of two or more greater than the equivalent dry deposition fluxes predicted by ADMS. Some of this is due to the latter using a wind variability model, but not all, as will be shown in what follows.

On the two crosswind rakes across the ground at $x = 140$ and 170 m from the inlet, the lateral spread of the plume is much reduced when compared with the ADMS predictions – something that the introduction of a wind variability model is intended to address.

4.3. Variable wind direction simulations

Zanetti (1990) notes that whilst instantaneous plume concentrations may be irregular, the time-averaged concentration profiles can be approximated by a Gaussian distribution in horizontal direction. It is then reasonable to assume that since the variation of wind direction forms a part of this irregularity, then the wind direction variation is Gaussian – an assumption which is also supported by the distribution of field measurements of wind direction change in Mahrt (2010) as we saw in Section 2.

In the present work, the mean wind direction, μ_{wd} was allocated a value of zero, aligned with the x-axis. Since the fetch represents a flat homogeneous terrain, changes in the direction of the wind were achieved by skewing the x and y-components of the inlet velocity on the three inlets seen in Fig. 3 by the desired angle. The limits of the directional variability were taken to be $\mu_{\text{wd}} \pm 3\sigma_{\delta\text{wd}}$, since over 99% of the area under a Gaussian distribution falls within three standard deviations of the mean. Thus, CFD simulations were carried out for evenly spaced

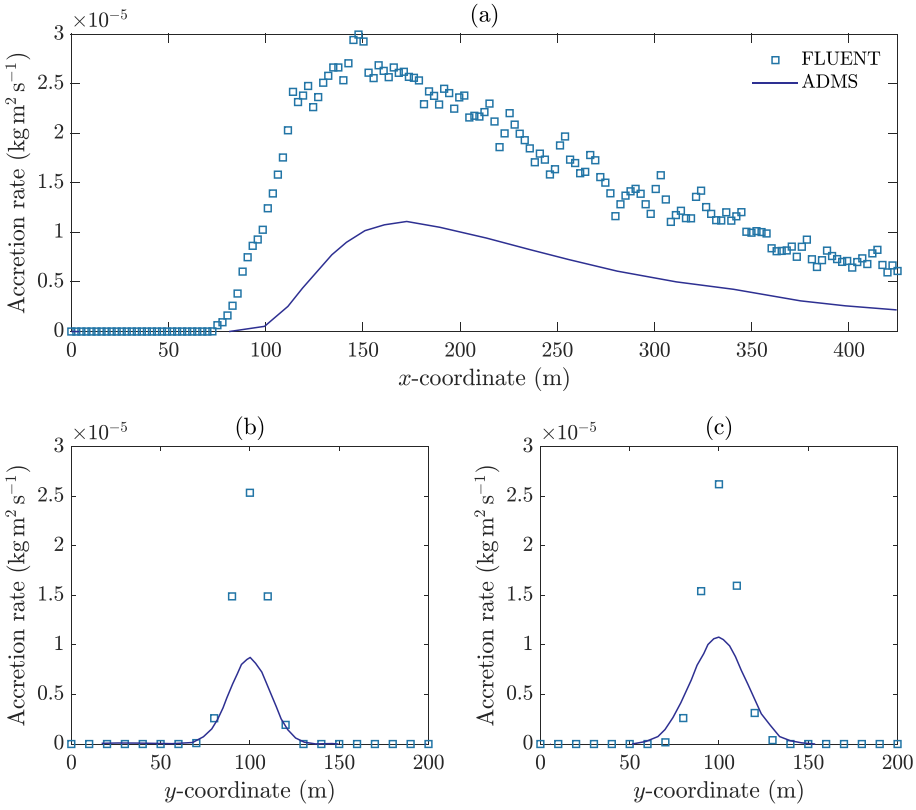

Fig. 5. Plots of accretion rate (dry deposition flux in ADMS) for the $\theta = 0^\circ$ case of a neutral ABL and $c_L = 0.30$ along (a) the centreline, $y = 0$ m. (b) $x = 140$ m, and (c) $x = 170$ m.

angular increments within this range. Both positive and negative angles were used because, despite the inherent symmetry in the plumes, the stochastic nature of the particle tracking algorithm suggested it was better to take this approach. Further, if the terrain were not flat and/or there were obstructions to the flow, this variation either side of the mean would be necessary.

The process of weighting the contribution of each of the directional variations including the mean wind to the resultant plume was automated in MATLAB according to

$$\overline{R_{\mathrm{acc}}} = \frac{\sum_{\theta=-3\sigma_{\delta\mathrm{wd}}}^{\theta=3\sigma_{\delta\mathrm{wd}}} p(\theta) R_{\mathrm{acc},\theta}}{\sum_{\theta=-3\sigma_{\delta\mathrm{wd}}}^{\theta=3\sigma_{\delta\mathrm{wd}}} p(\theta)}, \tag{34}$$

where $\overline{R_{\mathrm{acc}}}$ is the weighted average accretion rate, θ wind angle for each simulation number and $p(\theta)$ is the probability of occurrence of the wind direction θ. In equation (34), the denominator yields values very close to unity since the bulk of the normal distribution lies within these limits.

A quadrature is used to evaluate the definite integral of the Gaussian function at whatever increments of wind direction, $\delta\theta$, are being used

$$p(\theta) = \frac{1}{\sigma_{\delta\mathrm{wd}}\sqrt{2\pi}} \int_{\theta-\delta\theta}^{\theta+\delta\theta} \exp\left[-\frac{(\theta-\mu)^2}{2\sigma_{\delta\mathrm{wd}}^2}\right] \mathrm{d}\theta. \tag{35}$$

Quinn et al. (2001) noted that their use of nine values of wind direction fluctuations may not have been sufficient. So in the present work, tests were carried out to determine an optimal number of wind angles (and hence simulations) required to adequately account for directional variability, without compromising the accuracy of the method. To this end, increments of $\delta\theta = \sigma_{\delta\mathrm{wd}}$, $\sigma_{\delta\mathrm{wd}}/2$ and $\sigma_{\delta\mathrm{wd}}/4$ were used, creating sets of 7, 13 and 21 simulations respectively. In reality, this amounted to running 21 simulations and choosing a reduced subset from this larger set.

At the largest increment, $\delta\theta = \sigma_{\delta\mathrm{wd}}$, the scatter of accretion results was more pronounced as can be seen in Fig. 6. All increments appeared to be closely matched in terms of accretion predictions. Upon closer inspection, a variation of approximately 7% was observed between the weighted results of the $\sigma_{\delta\mathrm{wd}}$ set and the $\sigma_{\delta\mathrm{wd}}/2$ set beyond the accretion maxima. However the difference between the weighted results of the $\sigma_{\delta\mathrm{wd}}/2$ set and $\sigma_{\delta\mathrm{wd}}/4$ set was appreciably smaller at 1%. This suggests that 13 simulations are required for each mean wind direction to account for the variability in the wind direction about this mean. Results that are presented in Section 4.4 use the 13 simulation summation.

The difference between the locations of the concentration maxima was negligible for all increments and did not appear to be dependent on the size of the angular increments used to represent the wind variability for a given value of σ_{wd}. This sensitivity test was only carried out for the neutral boundary layer, because the calculated standard deviations for all three stability classes were of similar magnitudes (5° to 6°). It might be expected that for larger standard deviations, particularly those of a higher order of magnitude, increments of $\sigma_{\mathrm{wd}}/8$ may prove to be more appropriate.

Has the introduction of these multiple CFD simulations around each mean wind angle improved the agreement over using a single simulation? The weighted averaging process does indeed decrease the disagreement between the CFD predictions and the ADMS results. This can be seen in the reduction in the peak values from Figs. 5(a)–6(a). Also the lateral spread of the plume is greater once the weighted averaging process is introduced. Another benefit is seen in the reduced scatter in the accretion rates, a consequence of averaging a larger set of simulations. However, large differences persist: accretion rates are over-predicted by a factor of 2 and the point at which the plume first impacts the ground is far too close to the source for the CFD simulations.

4.4. Sensitivity to Lagrangian time scale constant

Maintaining the weighted wind direction method in what follows, the value of c_L was reduced from 0.30 to 0.15 (the default in FLUENT for

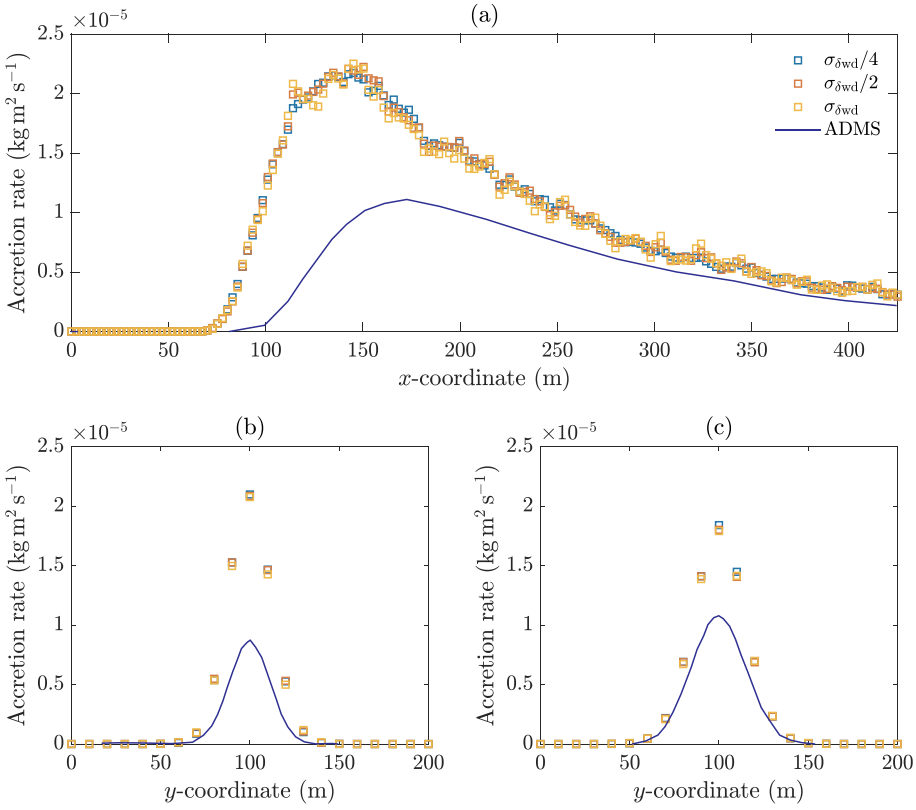

Fig. 6. Plots of accretion rate (dry deposition rate in ADMS) for various increments of σ_{wd} with a neutral ABL and $c_L = 0.30$ along (a) the centreline, $y = 0$ m. (b) $x =$ 140 m, and (c) $x = 170$ m.

the $k-\varepsilon$ model) and finally to 0.05 for the neutral and stable cases. Simulations for $c_L = 0.30$ for the unstable case are not available. This reduction should reduce the dispersion of the particulate plume in all three Cartesian directions equally (a consequence of Equation (13)). In what follows, first some general observations will be drawn in qualitative terms, followed by a discussion.

Continuing with the now familiar neutral case, Fig. 7 shows how the reduction in c_L modifies both the alongwind and crosswind ground level accretion rates. From plot (a) it becomes apparent that those simulations with $c_L = 0.05$ produce a plume that encounters the ground much closer to the ADMS model. Indeed, the location of the peak accretion rate and its value are closer with the lowest value of c_L. In terms of lateral spread, shown in plot (b), the lowest value of c_L produces the closest fit to the ADMS results, but there are still differences.

For a quantitative measure of performance, Table 4 shows the normalised mean square error (NMSE)

$$\mathrm{NMSE} = \frac{\overline{(X_F - X_A)^2}}{\overline{X_F}\cdot\overline{X_A}}, \tag{36}$$

where, in the present work, X_F and X_A are the FLUENT and ADMS predictions of accretion rate. The NMSE is calculated for both the centreline and crosswind ground level accretion rates. According to Hanna et al. (2004), if NMSE is 1, then the typical error equals the mean and if NMSE were 4, the error is twice the mean.

In terms of the NMSE for the neutral case, there is a clear improvement as c_L is reduced for both the alongwind and crosswind profiles.

Moving on to the stable case, seen in Fig. 8, the results show a marked improvement in agreement with ADMS predictions as c_L is reduced, in terms of where the plume encounters the ground, the location and magnitude of the peak and the downwind concentrations – shown in plot (a) – as compared to the ADMS simulations. Further, the agreement between the two modelling approaches in the crosswind spread and peak value at $x = 135$ m are improved for decreasing values of c_L. However, $x = 135$ m coincides with the location of the peak downwind concentration for the ADMS model, but occurs some distance after the peak in the FLUENT model, which must act as a rider to that observation. Nonetheless, the NMSE values for the stable case are a marked improvement on the neutral case, with the crosswind NMSE becoming very small as c_L is reduced to 0.05. The peak value of accretion rate is approximately three times higher than the neutral case, due to the fact that the particles are being advected more slowly in the stable case and thus can settle out more quickly. This can also be seen in the tail of the alongwind accretion rates, Figs. 7(a) and 8(a), where a higher proportion of the particles are still help aloft in the plume for the neutral case.

Table 4
Normalised mean square error of accretion rates for the stable, neutral and unstable cases along the centreline and in the crosswind direction.

	Centreline			Cross wind		
c_L	0.30	0.15	0.05	0.30	0.15	0.05
Stable	0.324	0.188	0.114	0.124	0.045	0.006
Neutral	1.015	0.344	0.198	0.967	0.341	0.162
Unstable	–	0.857	0.418	–	0.325	0.176

Finally for the unstable case, Fig. 9. The comparison bears similarities to the neutral case in that the plume encounters the ground before ADMS predicts it should, regardless of the value of c_L, plot (a). The lateral spread of the plume, plot (b), again indicates that the ADMS plume is more dispersed as it encounters the ground. This is confirmed with reference to Table 4, which shows that the NMSE for the unstable case can be reduced with the by reducing c_L, but the errors remain significant.

Having made these observations, some context is required. In the FLUENT DPM model, the accretion rate is a measure of the number of particles impacting on the ground over a given area. The particles arrive there because they are advected by the wind, are dispersed by the

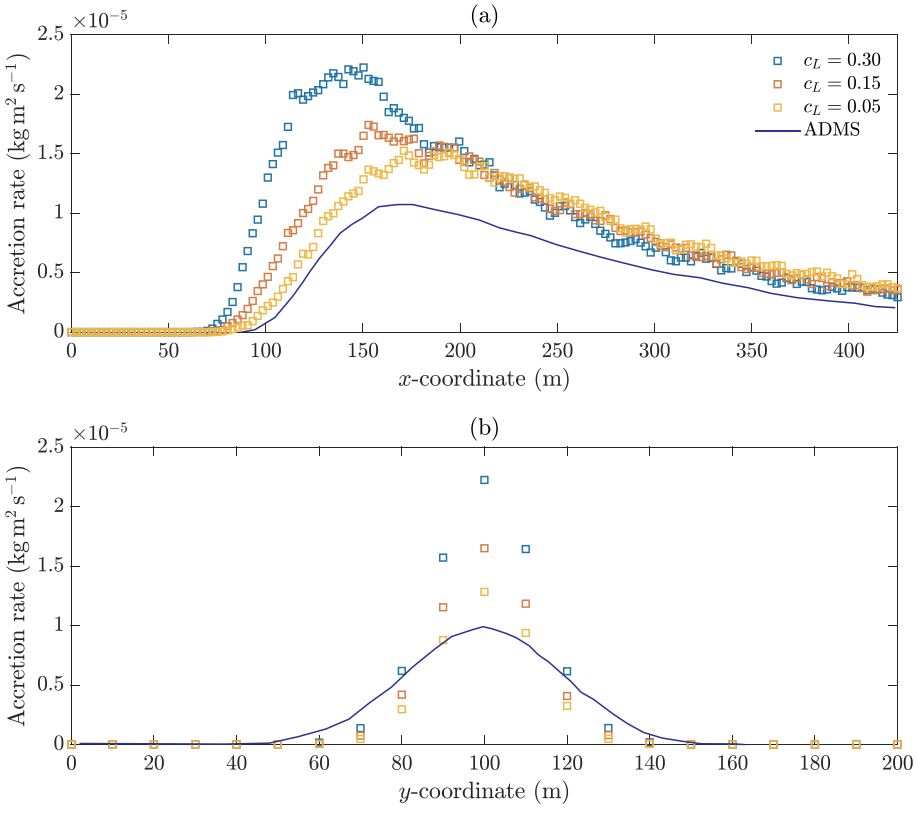

Fig. 7. Plots of accretion rates with different c_L values for the neutral case along a) the centreline, $y = 100$ m and (b) at $x = 150$ m.

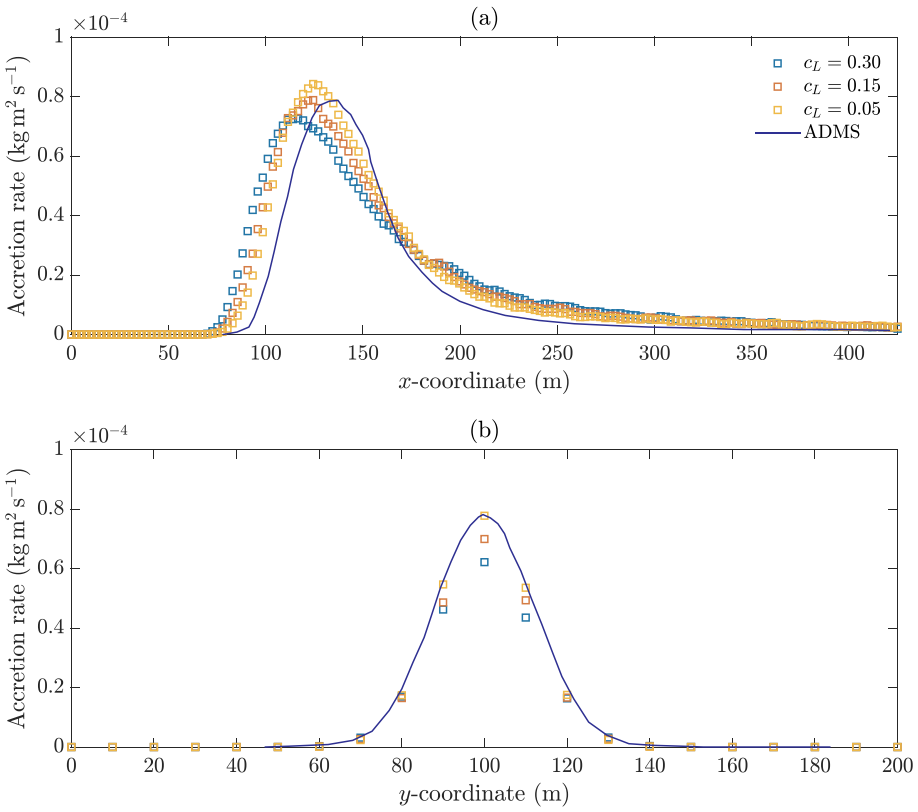

Fig. 8. Plots of accretion rates with different c_L values for the stable case along a) the centreline, $y = 100$ m and (b) at $x = 135$ m.

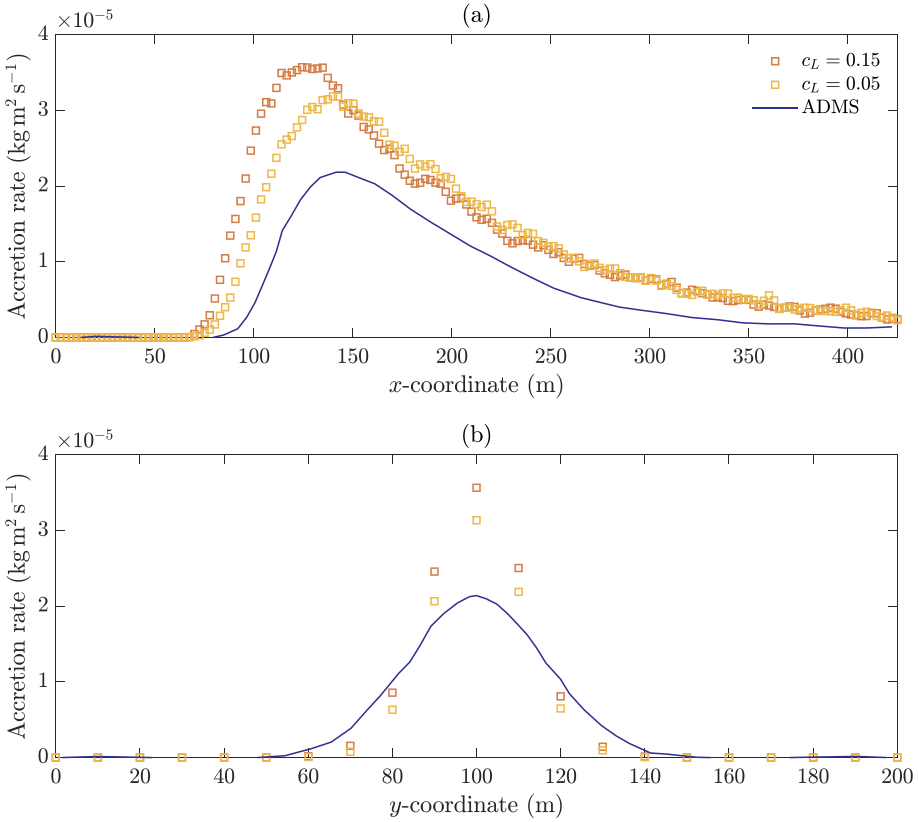

Fig. 9. Plots of accretion rates ith different c_L values for the unstable case along a) the centreline, $y = 100$ m and (b) at $x = 135$ m.

turbulence or settle out under the action of the gravitational field. These processes are also modelled in ADMS, albeit with quite different approaches. It could be argued that the advection and gravitational settling should be consistent between the two models, leaving the dispersion of the particulate plume the process which might generate discrepancies.

In Gaussian plume modelling, the dispersion parameters, $\sigma_y(x)$ and $\sigma_z(x)$, determine the lateral and vertical spread of the plume at some distance, x, downwind of the source. Over the distances considered in the present work, the lateral dispersion parameter is always greater than the vertical parameter, even for the case of a highly unstable environment. Hence, with the isotropic turbulence model used in the DPM model, Equation (13), it would be expected that, even if the levels of turbulence are modelled correctly using the Alinot and Masson (2005) approach, that vertical dispersion would be over-predicted and lateral dispersion under-predicted. The variable wind direction weighting should go some way to increase the latter, but the problem with the vertical dispersion remains.

Consider Fig. 8 where the best agreement between the two models is seen. In a stable environment, vertical mixing is largely suppressed and more of the horizontal dispersion of the plume aloft is due to the changing wind direction. The DPM model is based around the assumption of isotropic turbulence, which, in the stable environment, is lower, as shown in Fig. 4(c), which shows the non-dimensional turbulent kinetic energy for the three stability classes. Assuming then, as Riddle et al. (2004) do, that CFD simulations routinely under-predict lateral dispersion, the stable case should produce the best agreement with ADMS and this is because the variable wind direction correction should have the greatest effect here where the dispersion due to turbulence is lowest. Indeed, this is seen to be the case, with changes in c_L having the least impact on the accretion rates.

For the neutral and unstable cases, Figs. 7 and 9, we see similar trends, with a great deal of sensitivity to changes in c_L. In these cases, the plume impacts the ground earlier indicating that the vertical dispersion is being over-predicted while the lateral spread is too small, even with the variable wind direction taken into account. Again, this is symptomatic of the isotropic turbulence model being used. While the variable wind direction correction can increase the lateral spread of the accretion, the effect is not large enough in either the neutral or the stable case to completely compensate for the under-prediction of lateral spread in the DPM model.

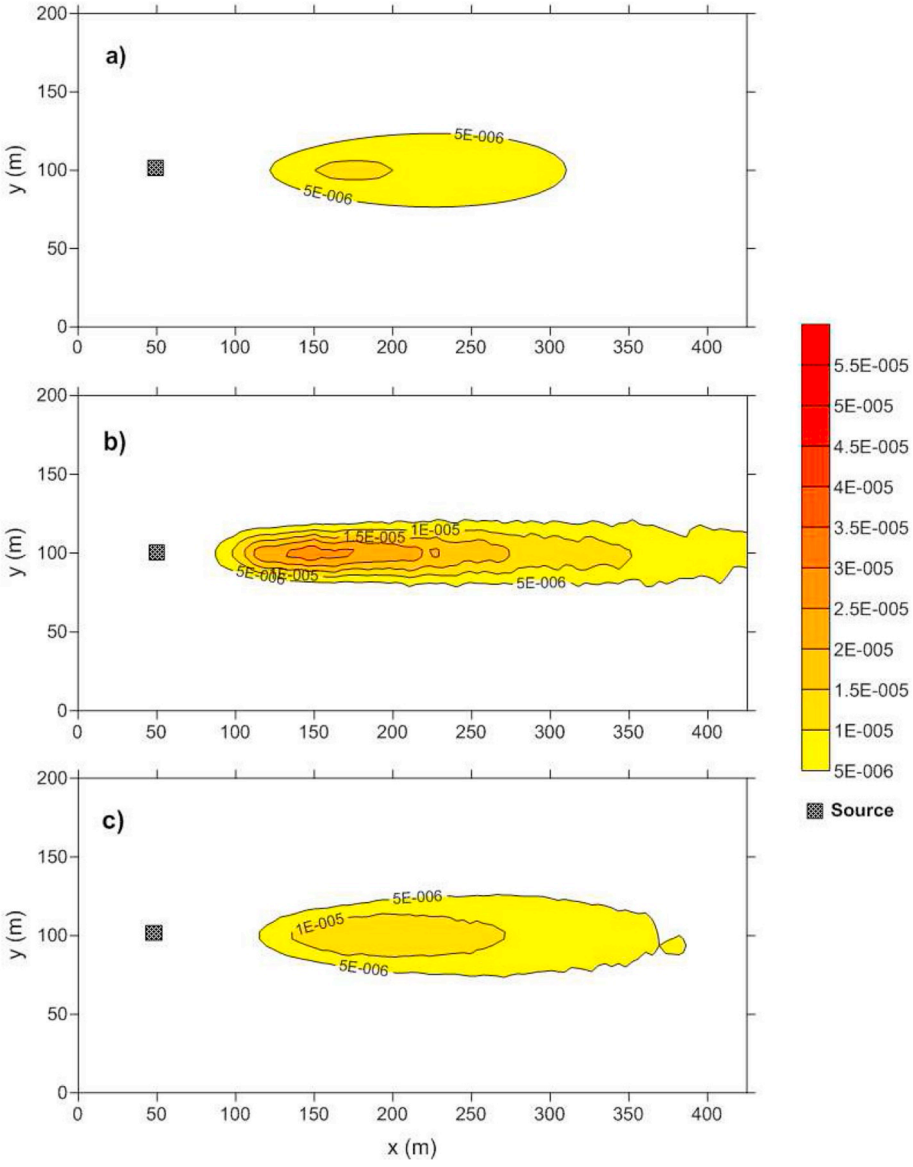

Fig. 10. Accretion rates (kgm^{-2}s^{-1}) for the neutral case for (a) ADMS, b) FLUENT with $c_L = 0.15$ and no wind variability correction and (c) FLUENT with $c_L = 0.05$ with wind variability correction.

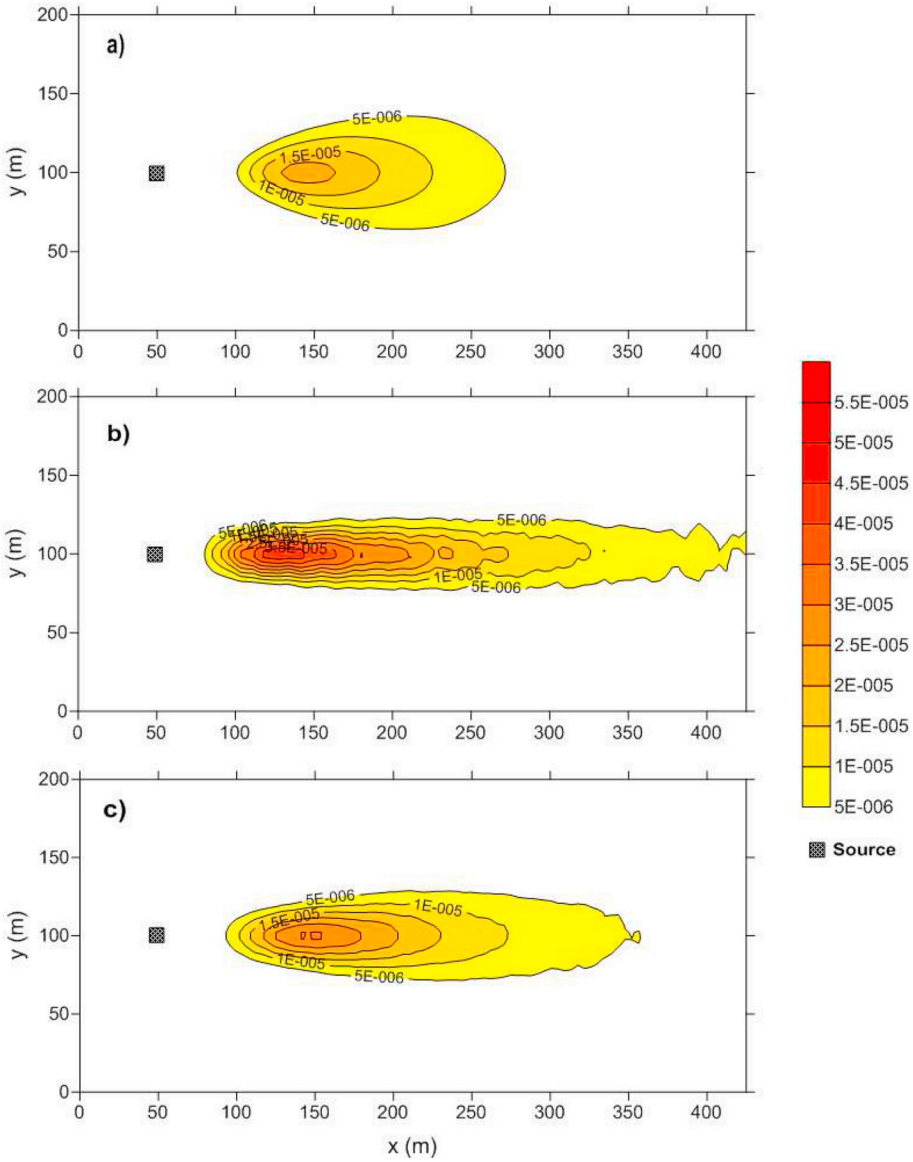

Fig. 11. Accretion rates ($kgm^{-2}s^{-1}$) for the stable case for (a) ADMS, b) FLUENT with $c_L = 0.15$ and no wind variability correction and (c) FLUENT with $c_L = 0.05$ with wind variability correction.

Finally, Figs. 10–12 show contours of accretion rates (dry deposition rates) for (a) ADMS, (b) FLUENT with the default value of $c_L = 0.15$ and no wind variability correction and (c) FLUENT with $c_L = 0.05$ with the wind variability correction. These figures tend to confirm the previous observations, with the stable case showing the closest agreement between the modified FLUENT and ADMS predictions. However, in all three cases, the qualitative agreement does improve with the reduction in c_L and the addition of the multiple wind direction cases.

5. Conclusions and further work

A methodology has been proposed and implemented to address the under-prediction of lateral plume spread in the FLUENT CFD model by introducing a wind direction variability correction according to the Moore (1976) generalization. ADMS, employs the Moore (1976) generalisation in its plume spread module, and has been used to evaluate any improvements in the lateral plume spread produced by the proposed methodology. The dispersion of particulates from an elevated emission source has been simulated using the FLUENT DPM model for three atmospheric stability classes and the accretion preditions have been compared to UK-ADMS dry-deposition predictions.

The results of this comparative study indicate that by incorporating wind direction variability through probability weighted simulations of wind direction variation, FLUENT predictions of lateral spreading of the particulate plume, improve appreciably. However, this modification to the standard approach of taking a single wind direction is not sufficient in itself. Further, the Langrangian integral time scale constant, c_L, must be modified from the default value as a means of altering the dispersive characteristics of the FLUENT plume, so that better agreement of FLUENT and ADMS predictions is obtained both in terms of the location and magnitude of peak deposition values. It is seen that a reduction in the constant corresponds to a decrease in accretion rates and a downwind shift of dust accretion.

However, the problem of using isotropic turbulence in the calculation of the random walks that the particle take in the DPM model remains. In future work, a more sophisticated approach is required, which is able to disaggregate the vertical and horizontal components of the turbulence, even when a RANS model is being used that assumes isotropic turbulence. To this end, the work of Philips et al. (2011) may point the way forward. The Buossinesq approximation can be used

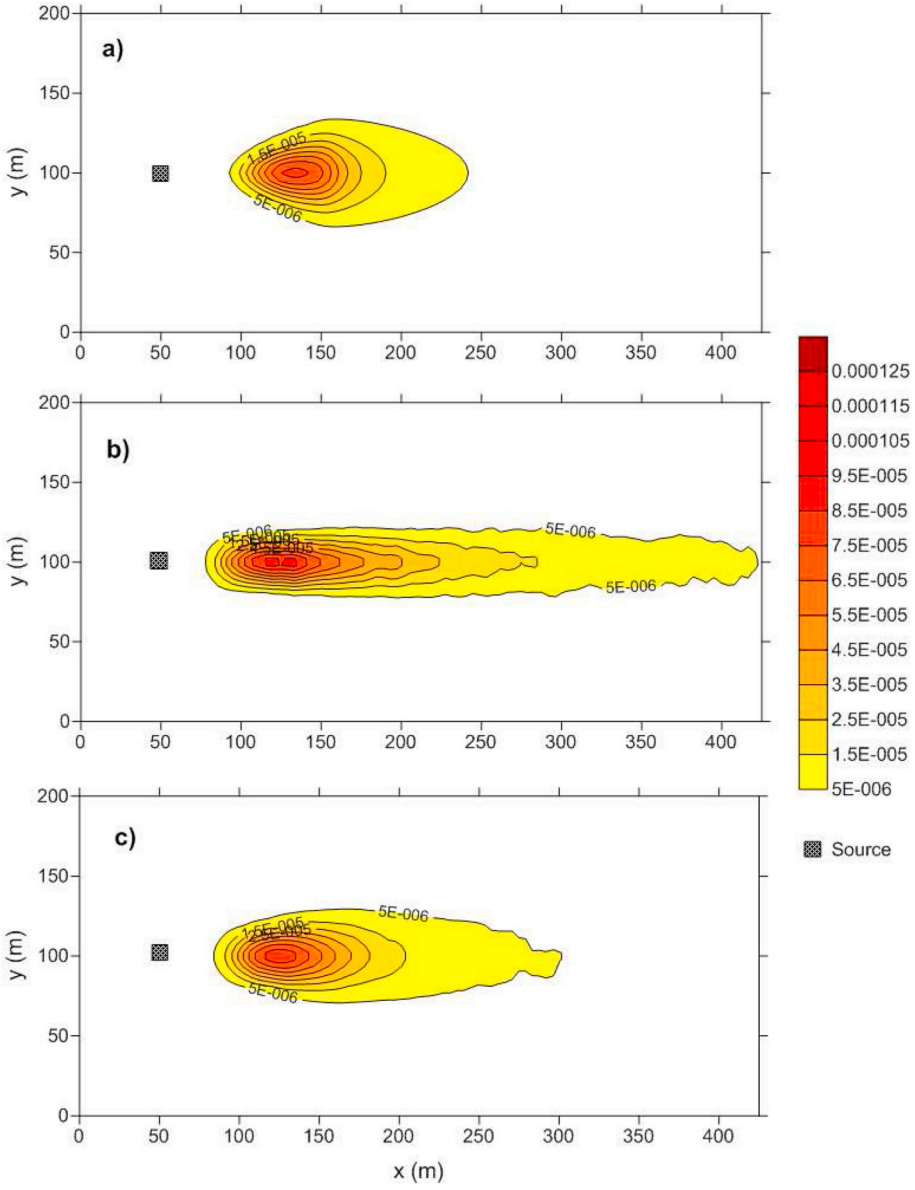

Fig. 12. Accretion rates ($kgm^{-2}s^{-1}$) for the unstable case for (a) UK-ADMS, b) FLUENT with $c_L = 0.15$ and no wind variability correction and (c) FLUENT with $c_L = 0.05$ with wind variability correction.

$$\overline{u_i{'}u_j{'}} = \frac{2}{3}k\delta_{ij} - \nu_t\left(\frac{\partial U_i}{\partial x_j} + \frac{\partial U_j}{\partial x_i}\right), \tag{37}$$

where U_i are the mean components of the velocity, k is the turbulent kinetic energy, δ_{ij} is the Kronecker delta and $\overline{u_i{'}u_i{'}}$, are the Reynolds stress components, the equivalent of σ_u in Equation (18). Using this approach, the nine main components of the Reynolds stress, $\overline{u_i{'}u_j{'}}$ can be calculated, based on the mean velocity and turbulence fields calculated by the flow solver.

For the case of a neutral ABL, the mean wind speed is

$$u(z) = \frac{u_*}{\kappa}\ln\left(\frac{z}{z_0}\right), \tag{38}$$

and

$$\frac{du}{dz} = \frac{u_*}{\kappa z}. \tag{39}$$

All other derivatives of the mean velocity vector are zero in this simplified case. The Reynolds stress tensor becomes

$$\overline{u_i{'}u_j{'}} = \begin{pmatrix} \frac{2}{3}k & 0 & -\nu_t\frac{u_*}{\kappa z} \\ 0 & \frac{2}{3}k & 0 \\ -\nu_t\frac{u_*}{\kappa z} & 0 & \frac{2}{3}k - \nu_t\frac{u_*}{\kappa z} \end{pmatrix}, \tag{40}$$

which shows that the turbulent component, $\overline{u_z{'}u_z{'}}$, is reduced in value using this approach. Thus, the vertical component of the random walk is suppressed.

Since the particle tracking is essentially a post-processing task, the variation in these components of the turbulence could be built into the particle tracking model to decrease the vertical component of dispersion relative to the horizontal rate. The derivatives of the mean velocity vector are available to the user in FLUENT via User-Defined Functions (UDFs) so this should be a relatively straightforward task to implement, regardless of the stability class of the atmosphere. This, coupled with the wind variability correction, could lead to improved predictions of

vertical and horizontal plume spread.

Declaration of competing interest

The authors declare that they have no known competing financial interests or personal relationships that could have appeared to influence the work reported in this paper.

CRediT authorship contribution statement

G.M.D. Joseph: Writing - original draft. **D.M. Hargreaves:** Writing - review & editing. **I.S. Lowndes:** Writing - review & editing.

Appendix A. Supplementary data

Supplementary data to this article can be found online at https://doi.org/10.1016/j.aeaoa.2020.100064.

References

Alinot, C., Masson, C., 2005. k-ε model for the atmospheric boundary layer under various thermal stratification. J. Sol. Energy Eng. 127, 438–443.

Anfossi, D., Oettl, D., Degrazia, G., Goulart, A., 2005. An analysis of sonic anemometer observations in low wind speed conditions. Boundary-Layer Meteorol. 114, 179–203.

Arya, S.P., 1995. Modeling and parameterization of near-source diffusion in weak winds. J. Appl. Meteorol. 34, 1112–1122.

Barthelmie, R.J., 1999. The effects of atmospheric stability on coastal wind climates. Meteorol. Appl. 6, 39–47.

Blocken, B., Stathopoulos, T., Carmeliet, J., 2007. CFD simulation of the atmospheric boundary layer: wall function problems. Atmos. Environ. 41, 238–252.

Countess, R., 2001. Methodology for Estimating Fugitive Windblown and Mechanically Resuspended Road Dust Emissions Applicable for Regional Scale Air Quality Modeling. Technical Report. Western Governors Association, Countess Environmental.

Cowherd, C., Grelinger, M., Gebhart, D., 2006. Development of an Emission Reduction Term for Near-Source Depletion. Research Institute for U.S. Army Engineering Research and Development Center, Construction Engineering Research. Technical Report. Prepared by Midwest.

Davies, B.M., Thomson, D.J., 1999. Comparisons of some parametrizations of wind direction variability with observations. Atmos. Environ. 33, 4909–4917.

Deaves, D.M., Lines, I.G., 1998. The nature and frequency of low wind speed conditions. J. Wind Eng. Ind. Aerod. 73, 1–29.

Degrazia, G., Anfossi, D., 1998. Estimation of the Kolmogorov constant C_0 from classical statistical diffusion theory. Atmos. Environ. 32, 3611–3614.

Di Sabatino, S., Buccolieri, R., Pulvirenti, B., Britter, R., 2007. Simulations of pollutant dispersion within idealised urban-type geometries with CFD and integral models. Atmos. Environ. 41, 8316–8329.

Gorlé, C., Van Beeck, J., Rambaud, P., Van Tendeloo, G., 2009. CFD modelling of small particle dispersion: the influence of the turbulence kinetic energy in the atmospheric boundary layer. Atmos. Environ. 43, 673–681.

Hanna, S.R., Hansen, O.R., Dharmavaram, S., 2004. FLACS CFD air quality model performance evaluation with Kit Fox, MUST, Prairie Grass, and EMU observations. Atmos. Environ. 38, 4675–4687.

Hargreaves, D.M., Wright, N.G., 2007. On the use of the k-ε model in commercial CFD software to model the neutral atmospheric boundary layer. J. Wind Eng. Ind. Aerod. 95, 355–369.

Isaksen, I.S.A., Granier, C., Myhre, G., Berntsen, T.K., Dalsøren, S.B., Gauss, M., Klimont, Z., Benestad, R., Bousquet, P., Collins, W., Cox, T., Eyring, V., Fowler, D., Fuzzi, S., Jöckel, P., Laj, P., Lohmann, U., Maione, M., Monks, P., Prevot, A.S.H., Raes, F., Richter, A., Rognerud, B., Schulz, M., Shindell, D., Stevenson, D.S., Storelvmo, T., Wang, W.C., van Weele, M., Wild, M., Wuebbles, D., 2009. Atmospheric composition change: climate–chemistry interactions. Atmos. Environ. 43, 5138–5192.

Jones, W., Launder, B., 1973. The calculation of low-Reynolds-number phenomena with a two-equation model of turbulence. Int. J. Heat Mass Tran. 16, 1119–1130.

Joseph, G., 2016. Improved Dust Dispersion Modelling for Surface Quarries: an Optimized RANS K-ε Approach. Ph.D. thesis. University of Nottingham.

Joseph, G., Lowndes, I., Hargreaves, D., 2018. A computational study of particulate emissions from Old Moor Quarry, UK. J. Wind Eng. Ind. Aerod. 172, 68–84.

Kaimal, J., Finnigan, J., 1994. Atmospheric Boundary Layer Flows, Their Structure and Measurement. Oxford University Press, New York, USA.

Lateb, M., Meroney, R.N., Yataghene, M., Fellouah, H., Saleh, F., Boufadel, M., 2016. On the use of numerical modelling for near-field pollutant dispersion in urban environments- A review. Environ. Pollut. 208, 271–283.

Lowndes, I.S., Silvester, S.A., Kingman, S.W., Hargreaves, D.M., 2008. The Application of an Improved Multi-Scale Computational Modelling Techniques to Predict Fugitive Dust Dispersion and Deposition within and from Surface Mining Operations.

Luketa-Hanlin, A., Koopman, R.P., Ermak, D.L., 2007. On the application of computational fluid dynamics codes for liquefied natural gas dispersion. J. Hazard Mater. 140, 504–517.

Mahrt, L., 2010. Surface wind direction variability. J. App. Meteorol. Climatol. 50, 144–152.

Michigan Department of Environmental Quality, 2004. Calculating Air Emissions for the Michigan Air Emissions Reporting System (MAERS).

Moore, D.J., 1976. Calculation of ground-level concentration for different sampling periods and source locations. Atmos. Pollut. 51–60.

Philips, D.A., Rossi, R., Iaccarino, G., 2011. The influence of normal stress anisotropy in predicting scalar dispersion with the v^2-f model. Int. J. Heat Fluid Flow 32, 943–963.

Quinn, A.D., Wilson, M., Reynolds, A.M., Couling, S.B., Hoxey, R.P., 2001. Modelling the dispersion of aerial pollutants from agricultural buildings – an evaluation of Computational Fluid Dynamics (CFD). Comput. Electron. Agric. 30, 219–235.

Richards, P., Hoxey, R., 1993. Appropriate boundary conditions for computational wind engineering models using the k-ε turbulence model. J. Wind Eng. Ind. Aerod. 46–47, 145–153.

Riddle, A., Carruthers, D., Sharpe, A., McHugh, C., Stocker, J., 2004. Comparisons between FLUENT and ADMS for atmospheric dispersion modelling. Atmos. Environ. 38, 1029–1038.

Silvester, S.A., Lowndes, I.S., Hargreaves, D.M., 2009. A computational study of particulate emissions from an open pit quarry under neutral atmospheric conditions. Atmos. Environ. 43, 6415–6424.

Sousa, J., Gorlé, C., 2019. Computational urban flow predictions with bayesian inference: validation with field data. Build. Environ. 154, 13–22.

Thomson, D.J., 1987. Criteria for the selection of stochastic models of particle trajectories in turbulent flows. J. Fluid Mech. 180, 529–556.

Toja-Silva, F., Chen, J., Hachinger, S., Hase, F., 2017. CFD simulation of CO_2 dispersion from urban thermal power plant: analysis of turbulent Schmidt number and comparison with Gaussian plume model and measurements. J. Wind Eng. Ind. Aerod. 169, 177–193.

Toja-Silva, F., Pregel-Hoderlein, C., Chen, J., 2018. On the urban geometry generalization for CFD simulation of gas dispersion from chimneys: comparison with Gaussian plume model. J. Wind Eng. Ind. Aerod. 177, 1–18.

Tominaga, Y., Stathopoulos, T., 2013. CFD simulation of near-field pollutant dispersion in the urban environment: a review of current modeling techniques. Atmos. Environ. 79, 716–730.

Vervecken, L., Camps, J., Meyers, J., 2013. Accounting for wind-direction fluctuations in Reynolds-Averaged simulation of near-range atmospheric dispersion. Atmos. Environ. 72, 142–150.

Vickers, D., Mahrt, L., Belušić, D., 2008. Particle simulations of dispersion using observed meandering and turbulence. Acta Geophys. 56, 234–256.

Watson, J., Chow, J., 2000. Reconciling Fugitive Dust Emissions Inventory and Ambient Source Contribution Estimates: Summary of Current Knowledge and Needed Research. Desert Research Institute, Energy and Environmental Engineering Centre. Technical Report.

Wise, D., Boppana, V., Li, K., Poh, H., 2018. Effects of minor changes in the mean inlet wind direction on urban flow simulations. Sustain. Cities Soc. 37, 492–500.

Woodward, J.L., 1999. Appendix A: Atmospheric Stability Classification Schemes. John Wiley and Sons, Inc., pp. 209–212

Zanetti, P., 1990. Air Pollution Modelling, Theories, Computational Methods and Available Software. Van Nostrand Reinhold, Southampton, Boston.